Global Optimization of Wing Aerodynamic Optimization Case Exhibiting Multimodality*

D.J. Poole †, C.B. Allen ‡, T.C.S. Rendall§

Department of Aerospace Engineering, University of Bristol, Bristol, BS8 1TR, U.K.

An investigation into an aerodynamic optimization benchmark case that exhibits multimodality is presented using a global optimization approach. The recently suggested case 6 of the AIAA Aerodynamic Design Optimization Discussion Group involves the drag minimization of a rectangular NACA0012 wing subject to lift and root bending moment, as well as other geometric constraints. In this paper, optimization of that case using a state-of-the-art constrained population-based global optimization framework is presented. Shape control is achieved via a hierarchical application of the radial basis function domain element approach. Three different fidelity of optimization cases are performed to investigate the multimodality of various aspects of the full problem, with four independent runs of each case being performed. When considering chord optimization, the optimizer converges to two independently identifiable minima with very similar performance. When adding dihedral and sweep variation, further multimodality is introduced, though this multimodality is reasonably well defined, with minima including forward and rearward sweep, and an upward and downward winglet. Introducing thickness variables leads to a highly multimodal problem due to the coupling between the chord and thickness variables. The theoretical minimum drag for this case is 24.7 counts, which a number of the runs get close to achieving.

I. Introduction and Background

Aerodynamic shape optimization (ASO) is the process used to optimize a given aerodynamic shape within a computational environment to improve on a design requirement. The aerodynamic model (normally a

*Originally presented as AIAA Paper 2017-4365 at 35th AIAA Applied Aerodynamics Conference, Denver, Colorado, June 2017.

†Senior Teaching Associate. Email: d.j.poole@bristol.ac.uk

‡Professor of Computational Aerodynamics. Email: c.b.allen@bristol.ac.uk

§Lecturer. Email: thomas.rendall@bristol.ac.uk

computational fluid dynamics (CFD) flow solver) is used to evaluate some metric against which to optimize called the objective, which in the case of ASO is an aerodynamic quantity, such as drag [1] or range [2], subject to a set of constraints which are usually aerodynamic or geometric. Along with the fluid flow model, the ASO framework requires a surface parameterization scheme which mathematically describes the aerodynamic shape being optimized by a series of design variables; changes in the design variables, which are made by a numerical optimization algorithm, result in changes in the aerodynamic surface. Numerous advanced optimizations using compressible computational fluid dynamics (CFD) as the aerodynamic model have previously been performed [3–7]. The authors have also presented work in this area, having developed a modularised, generic optimization tool, that is flow solver and mesh type independent, and applicable to any aerodynamic problem [8, 9].

A substantial amount of research has been published for a number of decades in the field of ASO; review-like works have been presented in parameterization [10], and optimizer performance [11, 12]. One primary issue in the development of the research field has been a lack of consistent benchmarking of individual ASO frameworks on unified test cases. As such, the AIAA Aerodynamic Design Optimization Discussion Group (ADODG)[a] was formed. As part of this, a number of inviscid and viscous aerofoil and wing benchmark optimization cases were suggested, with a number of research groups presenting results; see [13–21] for example.

Recently, a new benchmark case has been suggested. The case involves the drag reduction of a rectangular NACA0012 wing subject to a substantial number of aerodynamic and geometric constraints [22]. The primary reason for introducing this new problem is to investigate a benchmark case that appears to exhibit multimodality. Knowledge of this is extremely important as the degree of multimodality has a substantial implication on the choice of optimization algorithm. The most common type of optimization algorithm employed when solving ASO problems is a gradient-based approach, where the local sensitivities of the objective and constraints with respect to the design variables are used as a basis to construct a search direction. In the case of a unimodal problem (where there is a single optimum solution), a gradient-based method will terminate at the single optimum. On the other hand, in the presence of a multimodal problem, the gradient-based algorithm will terminate at the nearest local optimum along which the initial search direction drives it. Hence, the major problem is that termination of a gradient-based method is guaranteed to find a minimum, but there is no knowledge of whether this is the global minimum or a local minimum. If a global optimum is known to be needed, then a global optimization approach can be used. Global optimization methods are typically either: evolutionary algorithms (EAs), such as genetic algorithms (GA)[23] or differential evolution (DE)[24, 25], or; swarm intelligence algorithms (SIAs), such as particle swarm optimization (PSO)[26], ant colony optimization [27] or gravitational search algorithm [28]. Typically these use a population of individ-

[a] https://info.aiaa.org/tac/ASG/APATC/AeroDesignOpt-DG/default.aspx

uals who evolve or cooperate together in pursuit of the global optimum, which, while being ideal for global optimization, comes at the cost of a substantial increase in the number of CFD flow solutions required [29].

The degree of multimodality in the field of aerodynamic shape optimization is very problem dependent. For aerofoil optimization, it has been suggested that ASO problems exist that are unimodal [11] and multimodal[30, 31], while the same is true of wings exhibiting unimodality [6] and multimodality [11]. Furthermore, recently, aerodynamic topology optimization results have suggested multimodality for a number of supersonic flow problems [32]. Recently, a variety of takes of the optimization of ADODG case 6 have been presented that use a vortex-lattice code for lower fidelity results [33], as well as the requested Euler flow [34, 35], and also investigations of the wing in viscous flow [34, 36].

Due to the substantial cost of using a global optimization approach for an ASO problem, and the apparent lack of multimodality in a number of ASO problems, global optimizers have had only a small use in ASO, see[37–41] for example. However, to investigate the mutimodality of the ADODG multimodal benchmark problem, a state-of-the-art constrained global optimization framework [42] is employed here. The framework, which uses a parallel decomposition of the search agent population for efficient computation, has previously been used for drag minimization of aerofoils [1] and is used here for the wing optimization.

The remainder of the paper is organised as follows: in sections II and III, the optimization problem and ASO framework are outlined, respectively; analytical optimization studies are presented in section IV; aerodynamic optimization results are presented in section V; finally, conclusions are given in section VI.

II. Problem Definition

In this section, the overall problem is described. First, a generic form of a constrained optimization problem is given, followed by the aerodynamic optimization problem considered.

II.A. Constrained Optimization Problem Definition

A generic single-objective optimization problem optimizes an objective function, J, which is a function of a vector of D design variables, $\boldsymbol{\alpha}$, subject to a vector of inequality constraints, $\mathbf{g}$, and equality, $\mathbf{h}$, constraints. There are a total of G inequality and H equality constraints. Bound constraints are also included for completion, which state that the design variables must lie within the D-orthotope bounded region in $\Re^D$, called the design space, $\mathcal{S}$. Bound constraints can also be written as $\mathbf{L} \leq \boldsymbol{\alpha} \leq \mathbf{U}$ where $\mathbf{L}$ and $\mathbf{U}$ are D-long vectors and give the lower and upper bounds of the design space, outside of which, $J(\boldsymbol{\alpha})$ has an unknown solution. Commonly this type of problem is known as a constrained numerical optimization problem (CNOP),

which formally, is written as:

$$\begin{aligned} \underset{\boldsymbol{\alpha}\in\Re^D}{\text{minimise}} \quad & J(\boldsymbol{\alpha}) \\ \text{subject to} \quad & \mathbf{g}(\boldsymbol{\alpha}) \leq \mathbf{0} \\ & \mathbf{h}(\boldsymbol{\alpha}) = \mathbf{0} \\ & \boldsymbol{\alpha} \in \mathcal{S} \end{aligned} \tag{1}$$

The solution to a CNOP is the global optimum solution, $\boldsymbol{\alpha}^*$, that minimises the objective function:

$$J(\boldsymbol{\alpha}^*) \leq J(\boldsymbol{\alpha}) \ , \forall \boldsymbol{\alpha} \in \mathcal{F}$$

where $\mathcal{F}$ is the feasible region, which is the region in $\mathcal{S}$ where all the constraints are satisfied.

II.B. Aerodynamic Problem Definition

The aerodynamic optimization problem requires the drag minimization of a rectangular NACA0012 wing of full aspect ratio 6 (without wing-cap); the half-wing is shown in figure 1. The half-wing is composed of a rectangular NACA0012 section of span 3.0 and a rounded wing-cap of width 0.06, resulting in the overall semi-span of 3.06. The wing is in compressible, inviscid flow at $M_\infty = 0.5$ and is trimmed to a target $C_L = 0.2625$.

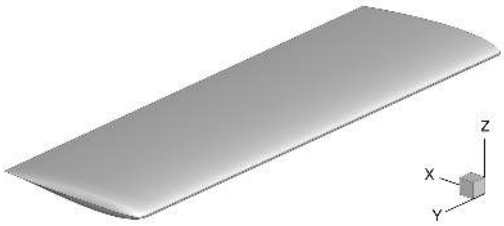

Figure 1: Rectangular NACA0012 wing

The objective is drag minimization subject to aerodynamic constraints on lift C_L, and root bending moment C_{M_x}, and geometric constraints on wing area S, internal volume V, twist γ, local chord $c(y)$, local thickness $t(y)$, sweep (local x deformation at the quarter-chord) $\Delta x_{qc}(y)$, semi-span s, dihedral (local z

deformation at the quarter chord) $\Delta z_{qc}(y)$, and angle of attack θ. The problem is given by:

$$\begin{aligned}
\underset{\boldsymbol{\alpha}\in\Re^D}{\text{minimise}} \quad & C_D \\
\text{subject to} \quad & C_L = 0.2625 \\
& C_{M_x} \leq 0.1069 \\
& S = S(\text{initial}) \\
& V \geq V(\text{initial}) \\
& -3.12^\circ \leq \gamma \leq 3.12^\circ \\
& 0.45 \leq c(y) \leq 1.55 \quad \forall y \in [0, s] \\
& 0.06 \leq t(y) \leq 0.18 \quad \forall y \in [0, s] \\
& -1 \leq \Delta x_{qc}(y) \leq 1 \quad \forall y \in [0, s] \\
& 2.46 \leq s \leq 3.67 \\
& -0.45 \leq \Delta z_{qc}(y) \leq 0.45 \quad \forall y \in [0, s] \\
& -3.0^\circ \leq \theta \leq 6.0^\circ
\end{aligned} \tag{2}$$

Assuming planar geometry and a thin wing, then it is possible to derive the theoretical optimum result for this case. Without the bending moment constraint, the well known optimal loading distribution for a finite span wing is the elliptic profile, first derived by Prandtl [43]:

$$\Gamma(\eta) = \Gamma_0 \sqrt{1 - \eta^2} \tag{3}$$

where Γ is the circulation, Γ_0 is a scaling and $\eta = y/s$ is the non-dimensional spanwise station. However, with a given bending moment constraint, then the elliptic distribution may not be obtainable, hence the solution of Jones [44] (which is a specific solution of a result later proved by Klein and Viswanathan [45]) becomes the optimal result:

$$\Gamma(\eta) = \Gamma_0 \left[(3 - 2\epsilon)\sqrt{1 - \eta^2} + 6(\epsilon - 1)\eta^2 \cosh^{-1}\left(\frac{1}{|\eta|}\right) \right] \tag{4}$$

where:

$$\epsilon = \frac{3\pi}{2} \frac{C_{M_x}}{C_L}$$

and Γ_0 is equivalent between equations 3 and 4, hence if $\eta = 0$ then for the elliptic distribution $\Gamma(0) = \Gamma_0$, whereas for the root bending moment constrained distribution $\Gamma(0) = \Gamma_0(3 - 2\epsilon)$.

A full discussion on optimal loadings subject to bending moment and lift constraints is comprehensively covered by Pate and German [46]. The elliptic loading and theoretical optimum loading given the root bending moment constraint are given in figure 2. Hence, it is clear that the elliptic profile is infeasible since the optimum profile shifts loading inboard to satisfy the moment constraint.

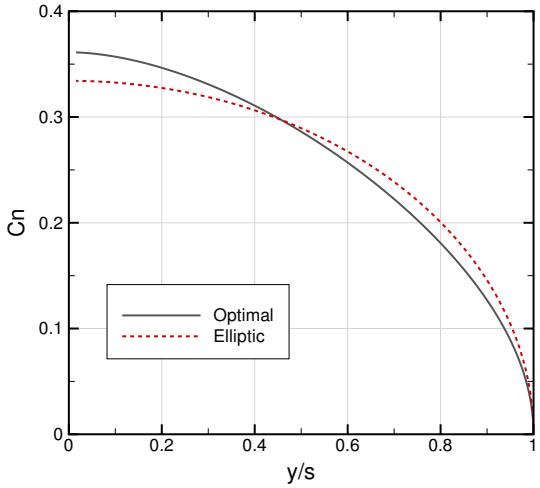

Figure 2: Theoretical optimum wing loading

The theoretical minimum induced drag can be calculated as:

$$C_{D_i} = \frac{C_L^2}{\pi AR}(1+\delta)$$

where $\delta = 8(\epsilon - 1)^2$, hence this varies with aspect ratio. Figure 3 gives the minimum induced drag for this (root bending moment) constrained problem for varying aspect ratio, also showing the minimum for the baseline aspect ratio, and aspect ratios at the minimum and maximum span. Hence, the theoretical minimum for this problem occurs at the maximum span, and is 24.7 counts.

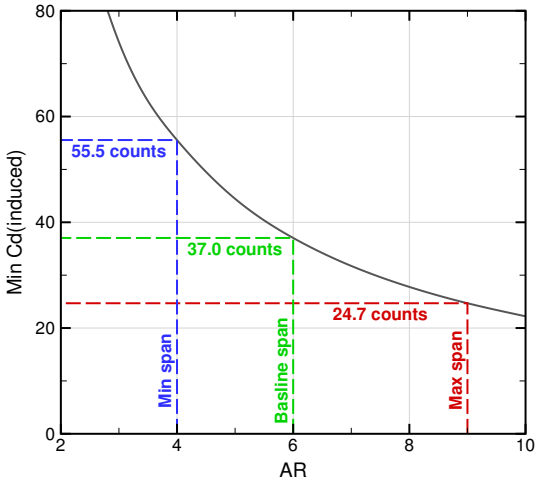

Figure 3: Theoretical optimum induced drag

III. Optimization Framework

In this section, the overall optimization framework used for performing the aerodynamic optimizations outlined later is described. A global optimization approach (as opposed to a gradient-based approach) with a reduced set of design parameters is considered. The flow solver and mesh, geometry and mesh control scheme, and optimizer are described individually below.

III.A. Flow Solver and Mesh

For optimization, it is important to be able to achieve sufficient resolution of the sensitivities of the objectives to changes in the aerodynamic surface. Here, this requires having a solver and a mesh that minimises any numerical noise or spurious drag.

The flow solver used is a structured multiblock, finite-volume, cell-centred scheme solving the compressible Euler equations in cartesian and rotating coordinate system. The convective terms are evaluated using the Jameson-Schmidt-Turkel (JST) scheme [47], chosen such that numerical drag is minimised. Multi-stage Runge-Kutta with local timestepping is used for time integration, and convergence acceleration is achieved through V- and W-cycle multigrid [48].

To ensure sufficient mesh resolution is used for the optimization, a grid convergence study is presented. A datum fine grid containing approximately 5.5m nodes in an eight-block structured C-mesh topology was generated [49]. Each block was subsequently coarsened in all three directions by a factor of two each time, leading to a medium mesh containing approximately 712k nodes and a coarse mesh containing approximately 95k nodes. Figure 4 shows the surface, wake and symmetry boundary of the three meshes. Table 1 gives the final drag values of the three meshes. Richardson extrapolation (see Roy [50], for example) is used on

the two finer meshes to obtain the grid converged drag value. The fine grid achieves a resolution of one drag count against the continuous drag value, however this comes at the expense of a substantial run-time. Since global optimization is being performed, where large numbers of flow solutions are required, the medium mesh appears to give the best trade-off of resolution and run-time and this is the one that is used for the optimizations.

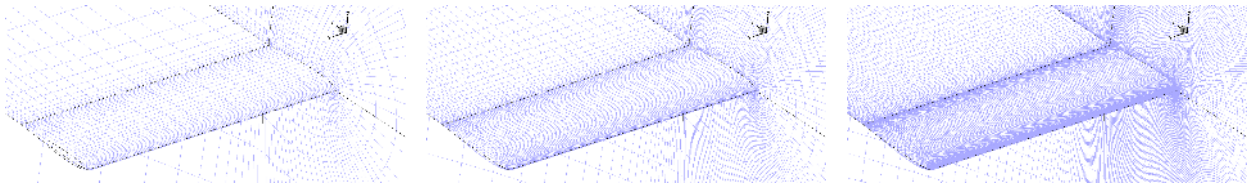

(a) Coarse (b) Medium (c) Fine

Figure 4: Mesh refinement study grids

Table 1: Baseline mesh convergence study (C_D in counts)

Grid	Nodes	C_D
Coarse	95,256	69.75
Medium	712,744	43.81
Fine	5,511,240	39.13
	∞	38.10

Figure 5 shows further views of the medium mesh that is used for optimization including the domain and boundaries, farfield mesh, surface mesh and chordwise planes. The mesh has a 129× 41 surface mesh, 33 nodes on either side of the wake, and 41 nodes between the inner and outer boundary.

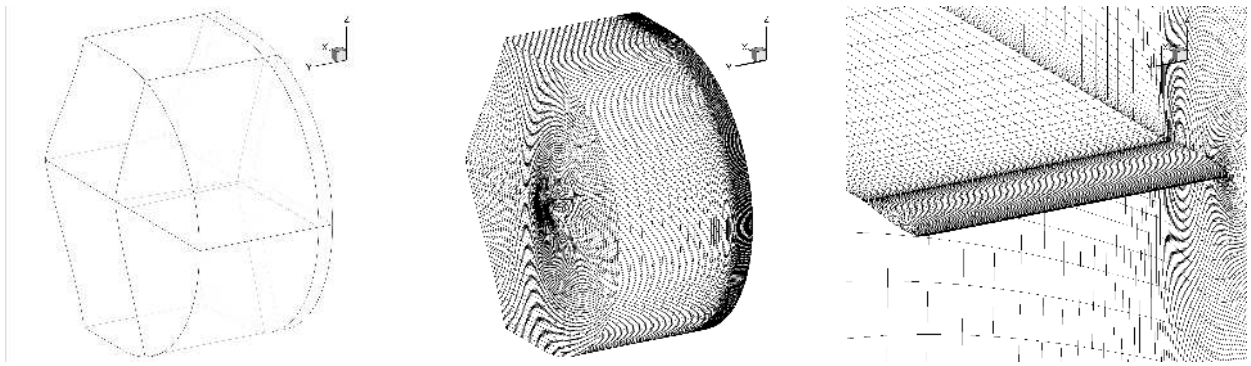

Figure 5: Eight-block wing mesh

III.B. Shape Control

The geometry and mesh control scheme must be flexible enough to allow sufficient design space investigation and efficient enough to maximise design space coverage with a minimum number of design parameters. The consideration of a global optimization approach necessitates the requirement for a minimum number of design variables to reduce computational burden as much as possible. The design variables used are primarily planform changes, which are from a mix of global planform deformations and local, sectional planform changes. Before describing the design variables, it is first necessary to describe the unified surface control and mesh deformation scheme.

For suitable surface control and mesh deformation, an efficient domain element shape parameterization method has been developed by the authors and presented previously for CFD-based shape optimization [8, 51]. The parameterization technique, surface control and volume mesh deformation all use radial basis functions (RBFs), wherein global interpolation is used to provide direct control of the design surface and the CFD mesh, which is deformed in a high-quality fashion [52, 53].

An RBF interpolation is of the form, $s(\mathbf{x})$. This is fit through a set of n data points, $\mathcal{X}$, where $\mathbf{x}_i \in \mathcal{X} \quad \forall i \in [1, \ldots, n]$, and $\mathbf{x} = \{x^{(1)}, \ldots, x^{(d)}\}$ is a vector of inputs in a d-dimensional space. The function to be modelled, $f(\mathbf{x})$, is known at each data point, which at the i-th data point has a scalar value, f_i. For a chosen basis function, ϕ, which is a function of the Euclidean distance, $\|\cdot\|$, between two vectors, the interpolation takes the form:

$$s(\mathbf{x}) = \sum_{i=1}^{n} \beta_i \phi(\|\mathbf{x} - \mathbf{x}_i\|) \tag{5}$$

where the coefficients, $\boldsymbol{\beta}$, are found by solving a linear system, $\mathbf{f} = \mathbf{M}\boldsymbol{\beta}$, constructed using the known data points to provide exact recovery of the data at the sites; hence $\mathbf{M}$ is a matrix of basis functions evaluated between the known sites.

When using RBF interpolation for unified shape control and mesh deformation, the known data sites are a small set of nc control points, where the i-th control point has a location in Cartesian space given by $\mathbf{x}_{c_i} = [x_{c_i}, y_{c_i}, z_{c_i}]$ which are commonly placed either close to or on the aerodynamic surface to give detailed control. Deformation of the control points leads to deformation of the mesh according to the RBF system, hence combinations of control point deformations act as design variables. Furthermore, the basis function in question is the radially-decaying Wendland C^2 [54] function, where the influence of the function is controlled by the support radius, outside of which the influence is zero.

For this work, to ensure smooth spanwise deformations, a hierarchical approach to constructing the design variables is achieved [55]. The overall set-up of control points and design variables is given in figure 6. A number of global deformations are combined with local deformations at a small number of spanwise

locations, with a blending function used to blend intermediate deformations between the spanwise locations. There are therefore two levels of control points; driver (which controls the deformation) and passenger (which acts to create smooth spanwise deformations). For this work, 24 driver control points at five equally spaced spanwise stations are employed for the higher level, while 24 passenger control points at four equally spaced spanwise stations between each of the higher level sections are used for the lower level. This leads to a total of 21 spanwise stations, each with 24 control points, all arranged in a lattice structure.

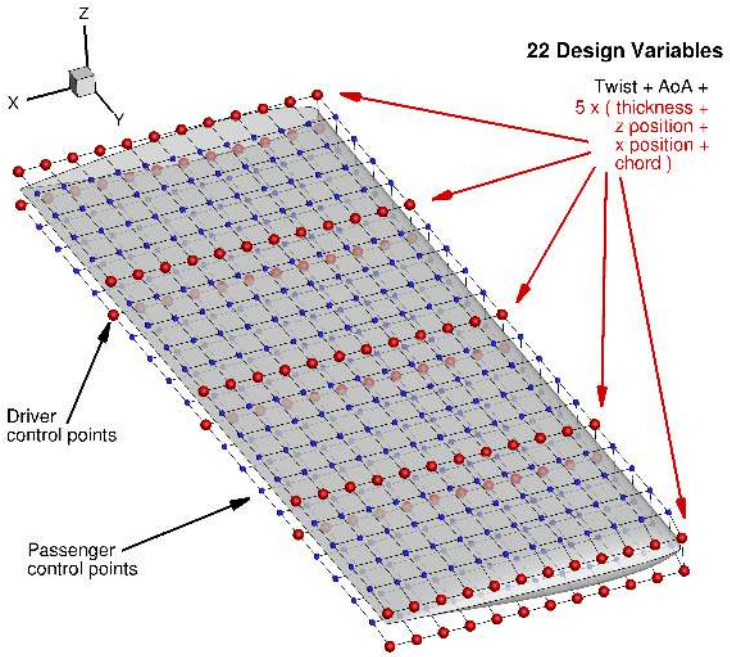

Figure 6: Hierarchical control points

The design variables are constructed to maintain maximum flexibility, while restricting the dimensionality which otherwise causes a global optimizer to have convergence issues. One global geometric design variable is used, which is linear twist. The linear twist is applied from zero at the root to the value of the design variable (which is the twist in degrees) at the tip. Hence, the local angle of rotation, γ, of a driver control point slice located at y_d is given by $\gamma(y_d) = \gamma y_d/s$. Local sectional geometric design variables for the driver control points are thickness, vertical deformation (to create dihedral), chordwise deformation (to create sweep) and chord. Span is allowed to vary, however this is not directly controlled by the optimizer, and instead it is calculated to ensure the wing area constraint is maintained. The global angle of attack is also allowed to vary within the limits set by the constraint, and this is applied by modifying the freestream conditions. This leads to a total of 22 design variables.

Deformations of the passenger control points are determined using the driver control points either side of a passenger's spanwise station. The passenger deformation is therefore a partition of unity blending between the deformations at the preceding and succeeding driver spanwise station. Using a partition of unity blending

has the advantage of first, being able to recover global deformations (such as a global thickness change) from local deformations, and second, providing smooth spanwise blending between a small set of driver control points. To define deformations of a slice of passenger control points, Δ_p, then the deformations of the slices of driver control points on either side of the passenger slice (Δ_d and Δ_{d+1}) are blended as:

$$\Delta_p = \Delta_d \cos^2\left(\frac{\pi\lambda}{2}\right) + \Delta_{d+1} \sin^2\left(\frac{\pi\lambda}{2}\right)$$

where $\lambda = (y_p - y_d)/(y_{d+1} - y_d)$. Hence, it can be seen that if the driver deformations are equivalent ($\Delta_d = \Delta_{d+1}$) then no matter the location of any passenger slice (assuming $y_d < y_p < y_{d+1}$) the deformation of the passenger slice will be the same as the driver deformations.

Figure 7 shows an example of an increase in the local chord on the second driver spanwise station with no other changes versus adding a decrease in the local chord on the third spanwise station, clearly showing the positive blending that is occurring to ensure a smooth chord distribution.

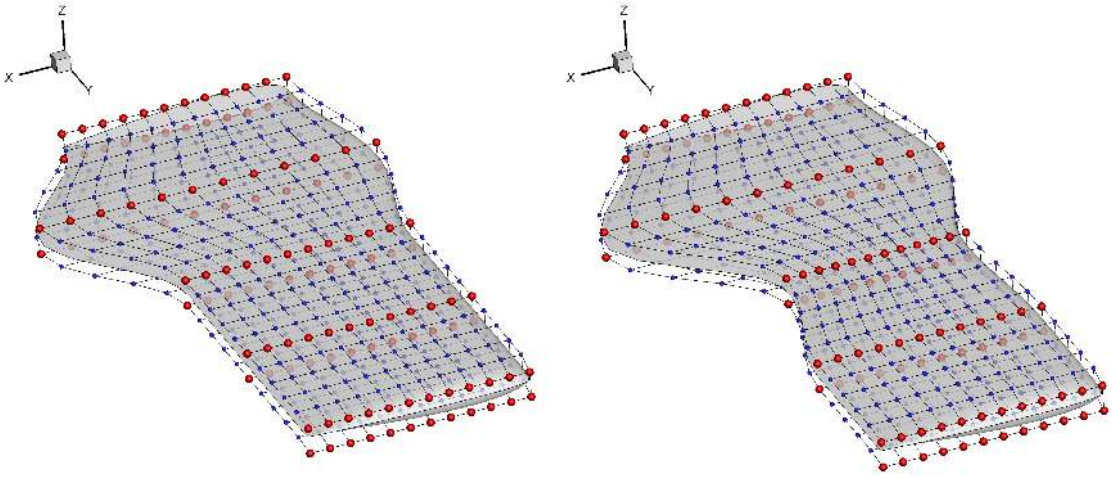

(a) Positive (b) Positive and negative

Figure 7: Chord change design variables

III.C. Optimizer

A global optimization approach is considered here, as opposed to a gradient-based approach. While global optimization can often be more expensive than performing gradient-based optimization, it is more likely to locate a globally optimal solution in a multimodal design space. The optimization framework has been developed by the authors, and shown to be effective an optimizing benchmark analytical problems [42] as well as transonic aerofoil problems [1].

The global optimization algorithm used is an agent-based method, where a population of agents are used to traverse the design space in search of a solution. The location of the n-th agent (which is an

individual within a population of N agents) at the t-th iteration within the search space of D design variables is $\boldsymbol{\alpha}_n(t) = [\alpha_n^{(1)}(t), \alpha_n^{(2)}(t), \ldots, \alpha_n^{(D)}(t)]^T$, and in an agent-based optimization algorithm moves to a new location, in the d-th dimension, at the next iteration of the search by:

$$\alpha_n^{(d)}(t+1) = \alpha_n^{(d)}(t) + v_n^{(d)}(t) \tag{6}$$

where $\mathbf{v}_n(t)$ is the vector of location deformations, which is more commonly termed a particle's velocity, the determination of which separates various agent-based methods.

A hybrid of the particle swarm optimization (PSO) [26], and the gravitational search algorithm (GSA) [28] has been developed and used here such that the memory qualities of PSO complement the global transfer of data that occurs in GSA to obtain a highly efficient global search algorithm. Furthermore, the design space exploration capabilities of PSO are combined with the optima exploitation capabilities of GSA to provide an algorithm that can both explore the design space and exploit the global optimum within it. The velocity of particles is calculated as:

$$v_n^{(d)}(t) = r_n v_n^{(d)}(t-1) + a_n^{(d)}(t) \tag{7}$$

where r_n is a uniformly distributed random number on the interval $[0, 1]$, and $\mathbf{a}_n$ is the particle's 'acceleration', which is a blend of PSO and GSA components:

$$a_n^{(d)}(t) = W a_{n,pso}^{(d)}(t) + (1-W) a_{n,gsa}^{(d)}(t) \tag{8}$$

where $\mathbf{a}_{n,pso}(t)$ and $\mathbf{a}_{n,gsa}(t)$ are the PSO and GSA constituents of the acceleration respectively, and W is a blending constant used to balance the qualities of PSO and GSA. Setting $W = 1$ means the search is driven by only PSO, while setting $W = 0$ means the search is driven by only GSA. To obtain a good balance, 0.5 is used in this work. The acceleration due to PSO is:

$$a_{n,pso}^{(d)}(t) = c_1 r_{1_n}(p_n^{(d)}(t) - \alpha_n^{(d)}(t)) + c_2 r_{2_n}(s^{(d)}(t) - \alpha_n^{(d)}(t)) \tag{9}$$

where c_1 is the cognitive constant, c_2 is the social constant, r_{1_n} and r_{2_n} are independent uniformly distributed random numbers on the interval $[0, 1]$ for each individual each iteration, $\mathbf{p}_n(t)$ is the individual's best location found so far, and $\mathbf{s}(t)$ is the global (swarm's) best location found so far. The acceleration due to GSA is given as:

$$a_{n,gsa}^{(d)}(t) = F_n^{(d)}(t)/M_n(t) \tag{10}$$

where $\mathbf{F}_n(t)$ is the forcing vector calculated using Newtonian mechanics and $M_n(t)$ is the particle mass, which is proportional to the fitness of the particle relative to all other particles (particles with a low objective function have a high mass and *vice versa*). A comparison of the update approaches between PSO and GSA is given in figure 8.

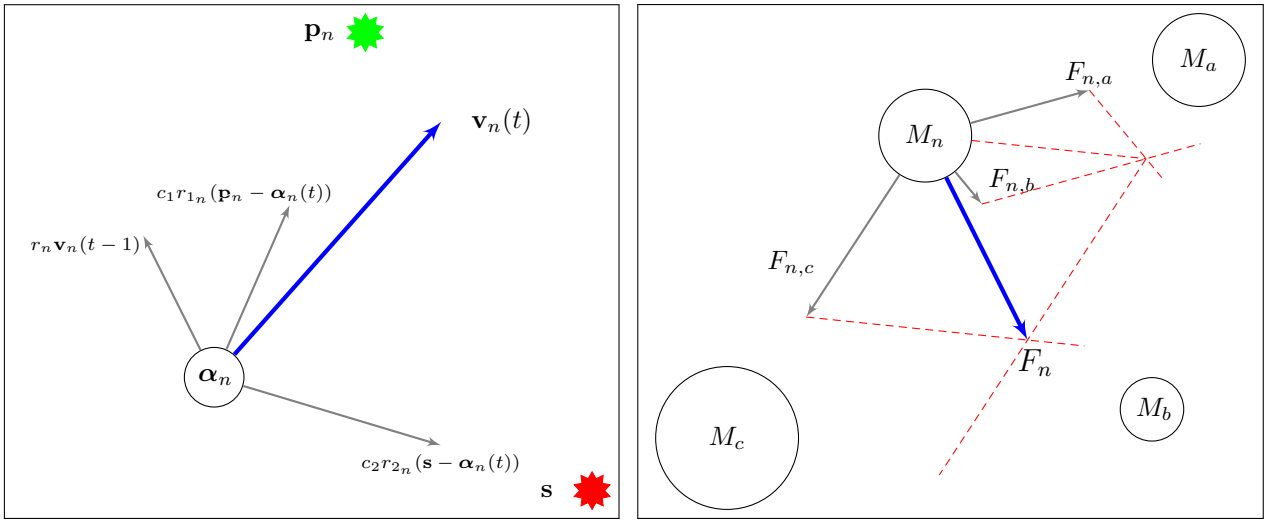

(a) PSO (b) GSA

Figure 8: Comparison of PSO and GSA update frameworks.

Constraints are not directly handled in the PSO or GSA algorithms, hence the separation-sub-swarm (3S) [42] constraint handling method is applied. The 3S method is a constraint handling framework that can be applied to any swarm intelligence algorithm and works by splitting the overall population into two independent swarms every iteration – one swarm containing all of the feasible particles at that iteration (all constraints are satisfied) and one containing all of the infeasible particles at that iteration (at least one constraint is violated). The swarms then independently solve a different objective function, where the objective function of a particle ζ is determined by:

$$\zeta(\boldsymbol{\alpha}) = \begin{cases} J(\boldsymbol{\alpha}) & \text{if } \phi(\boldsymbol{\alpha}) = 0 \\ \phi(\boldsymbol{\alpha}) & \text{else} \end{cases} \tag{11}$$

where ϕ is the sum of the constraint violations:

$$\phi(\boldsymbol{\alpha}) = \sum_{i=1}^{G} \max[0, g_i(\boldsymbol{\alpha})] + \sum_{j=1}^{H} |h_j(\boldsymbol{\alpha})| \tag{12}$$

Hence, the infeasible particles have the objective of minimizing the constraint violation and therefore trying to find the feasible region whereas the feasible particles are minimizing the objective that is to be solved for. Updates to the swarm's and an individual's best location are performed using a binary tournament selection

[56], which is achieved via the domination operator; given two locations within the design space, $\boldsymbol{\alpha}_a$ and $\boldsymbol{\alpha}_b$:

$$\boldsymbol{\alpha}_b \mapsto \boldsymbol{\alpha}_a \Leftrightarrow \boldsymbol{\alpha}_a \prec \boldsymbol{\alpha}_b \tag{13}$$

where

$$\boldsymbol{\alpha}_a \prec \boldsymbol{\alpha}_b \Leftrightarrow \begin{cases} J(\boldsymbol{\alpha}_b) < J(\boldsymbol{\alpha}_a) \text{ and } \phi(\boldsymbol{\alpha}_a), \phi(\boldsymbol{\alpha}_b) = 0 \\ \phi(\boldsymbol{\alpha}_b) = 0 \text{ and } \phi(\boldsymbol{\alpha}_a) > 0 \\ \phi(\boldsymbol{\alpha}_b) < \phi(\boldsymbol{\alpha}_a) \text{ and } \phi(\boldsymbol{\alpha}_a), \phi(\boldsymbol{\alpha}_b) > 0 \end{cases} \tag{14}$$

Bound constraints are handled by placing a particle back in its previous position if it violates the bound constraints i.e. is outside the design space.

III.D. Optimization Problem Definition

The aerodynamic problem definition has previously been outlined, however the problem definition that the optimizer deals with is slightly different. The reason for these differences is due to the way the design variables have been constructed. For example, explicit local and global planform changes are specified by design variables, hence, to avoid the over-specification of the problem (too many constraints), many of the linear constraints outlined in equation 2 can be converted to bound constraints. This improves performance of the optimizer.

Due to the complicated nature of the full problem, it is useful to consider a number of simpler problems before the full optimization problem is considered. In all optimizations, the span is calculated after the planform deformations to ensure the projected area constraint is satisfied. Also, to give the optimizer full flexibility, the lift constraint is implemented as an inequality constraint with the angle of attack as a variable. The twist variable is also always employed. Three different optimization problems are performed, termed cases A, B and C, the designation of which are described below. Regarding cost, due to using a global optimizer, assuming the cost of evaluating J is large (which in this case it is) and that the optimizer is run for a fixed maximum number of iterations, the variation in the overall cost due to different numbers of design variables is negligible. Hence, the difference in cost between cases A, B and C is negligible.

To investigate the modality of the problem, four independent optimization runs for each case are performed. Hence, there are four different initial distributions of particles, which are randomly positioned within the design space. Furthermore, due to the random terms in the optimizer update equations, the stochastic nature of the optimizer means no two runs are repeatable. The general trend that is being investigated is that of whether the independent optimization runs converge to similar objective functions but at individually identifiable locations in the design space.

III.D.1. Case A: Chord Optimization

Initially, optimization using chord changes are considered in isolation (along with angle of attack for trimming and twist). The theoretical optimum described above assumes planar geometry, so results close to this optimum should be attainable with chord variations only. The design variable specification is as follows:

- α_1 - angle of attack
- α_2 - linear twist
- α_3 to α_7 - chord changes of each section of driver control points

All constraints are transformed into the standard form given in equation 1, so the optimization problem being solved by the optimizer is:

$$\begin{aligned}
\underset{\boldsymbol{\alpha}\in\Re^D}{\text{minimise}} \quad & C_D \\
\text{subject to} \quad & 0.2625 - C_L \leq 0 \\
& C_{M_x} - 0.1069 \leq 0 \\
& V(\text{initial}) - V \leq 0 \\
& 2.46 - s \leq 0 \\
& s - 3.67 \leq 0 \\
& \\
& 3.0 \leq \alpha_1 \leq 6.0 \\
& -3.12 \leq \alpha_2 \leq 3.12 \\
& 0.45 \leq \alpha_i \leq 1.55 \quad \forall i \in [3, 7]
\end{aligned} \tag{15}$$

III.D.2. Case B: Planar and Non-Planar Optimization

Second, planar and non-planar deformations of the wing are introduced. Again, close to the theoretical optimum should be attainable since the design space of case A is entirely enclosed within the design space of case B. The design variable specification is as follows:

- α_1 - angle of attack
- α_2 - linear twist
- α_3 to α_7 - z-deformation of each section of driver control points
- α_8 to α_{12} - x-deformation of each section of driver control points

- α_{13} to α_{17} - chord changes of each section of driver control points

The root must remain fixed in the $x-z$ plane so α_3 and α_8 are set to zero in the optimizer to ensure this. Again, all constraints are transformed into the standard form, so the optimization problem being solved by the optimizer is:

$$\begin{aligned}
\underset{\boldsymbol{\alpha}\in\Re^D}{\text{minimise}} \quad & C_D \\
\text{subject to} \quad & 0.2625 - C_L \leq 0 \\
& C_{M_x} - 0.1069 \leq 0 \\
& V(\text{initial}) - V \leq 0 \\
& 2.46 - s \leq 0 \\
& s - 3.67 \leq 0 \\
& \\
& 3.0 \leq \alpha_1 \leq 6.0 \\
& -3.12 \leq \alpha_2 \leq 3.12 \\
& -0.45 \leq \alpha_i \leq 0.45 \quad \forall i \in [3,7] \\
& -1 \leq \alpha_i \leq 1 \quad \forall i \in [8,12] \\
& 0.45 \leq \alpha_i \leq 1.55 \quad \forall i \in [13,17]
\end{aligned} \tag{16}$$

III.D.3. Case C: Full Optimization

Finally, the full optimization problem is considered. Thickness changes are now introduced. The design variable specification is as follows:

- α_1 - angle of attack
- α_2 - linear twist
- α_3 to α_7 - thickness changes of each section of driver control points
- α_8 to α_{12} - z-deformation of each section of driver control points
- α_{13} to α_{17} - x-deformation of each section of driver control points
- α_{18} to α_{22} - chord changes of each section of driver control points

Again, the root must remain fixed in the $x-z$ plane so α_8 and α_{13} are set to zero in the optimizer to ensure this. The optimization problem being solved by the optimizer is:

$$\begin{aligned}
\underset{\boldsymbol{\alpha}\in\Re^D}{\text{minimise}} \quad & C_D \\
\text{subject to} \quad & 0.2625 - C_L \leq 0 \\
& C_{M_x} - 0.1069 \leq 0 \\
& V(\text{initial}) - V \leq 0 \\
& 2.46 - s \leq 0 \\
& s - 3.67 \leq 0 \\
& \\
& 3.0 \leq \alpha_1 \leq 6.0 \\
& -3.12 \leq \alpha_2 \leq 3.12 \\
& 0.06 \leq \alpha_i \leq 0.18 \quad \forall i \in [3,7] \\
& -0.45 \leq \alpha_i \leq 0.45 \quad \forall i \in [8,12] \\
& -1 \leq \alpha_i \leq 1 \quad \forall i \in [13,17] \\
& 0.45 \leq \alpha_i \leq 1.55 \quad \forall i \in [18,22]
\end{aligned} \tag{17}$$

IV. Analytical Optimization

Before progressing to performing aerodynamic optimization, it is worth considering the effect of running the optimizer on an analytical problem which has similar characteristics to the aerodynamic problems. The assumption with running the optimizer multiple times on the aerodynamic problem is that if there is a multimodal design space, that the multiple optima will be all close to global, that is, for a number of global optima $J(\mathbf{x}^{*1}) \approx J(\mathbf{x}^{*2}) \approx \ldots$ and that $\mathbf{x}^{*1} \neq \mathbf{x}^{*2} \neq \ldots$. To test the assumption that the optimizer will converge to different optima in independent tests in the event of multiple global optima being present, analytical optimization is considered.

The optimization problem considered is one that is constructed from the multimodal test problem generator of Deb and Saha [57]. This test function generator is a means to create a single objective problem, which is a hypersphere, subject to any number of hyperellipsoid constraints up to a maximum of the dimension of the problem. A simple two-dimensional, single constraint problem is considered to illustrate the assumptions

made:

$$\begin{aligned} \underset{\boldsymbol{\alpha}\in\Re^2}{\text{minimise}} \quad & \alpha_1^2 + \alpha_2^2 \\ \text{subject to} \quad & 4 - \alpha_1^2 - 4\alpha_2^2 \leq 0 \\ & -3 \leq \alpha_i \leq 3 \quad \forall i \in [1,2] \end{aligned} \tag{18}$$

Hence the objective is simply the sphere function with a constraint requiring that the solution lie on or outside an ellipse with centre $(0,0)$, major axis length 2 and minor axis length 1. This problem has two solutions at $(0,\pm 1)$ each with $J = 1.0$.

To demonstrate the characteristics of the optimizer when run on this function, the convergence of the particles in the search space for two independent runs are given in figure 9. Hence, it has been demonstrated that for two independent runs of the optimizer, that convergence to two different global optima can be achieved. Furthermore, it is clear that the optimization framework has performed well, resulting in a converged population of particles on a single global optimum. This is a result also repeated when tested on a much larger suite of analytical functions [42].

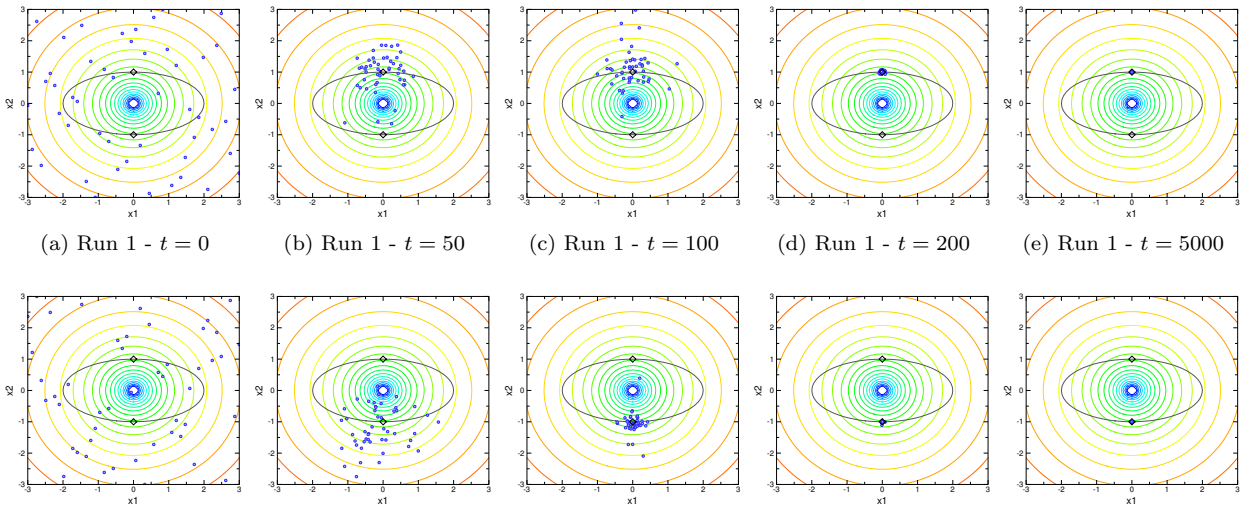

(a) Run 1 - $t = 0$ (b) Run 1 - $t = 50$ (c) Run 1 - $t = 100$ (d) Run 1 - $t = 200$ (e) Run 1 - $t = 5000$

(f) Run 2 - $t = 0$ (g) Run 2 - $t = 50$ (h) Run 2 - $t = 100$ (i) Run 2 - $t = 200$ (j) Run 2 - $t = 5000$

Figure 9: Particle convergence on analytical problem

V. Aerodynamic Optimization Results

In this section, results of the optimization of the NACA0012 rectangular wing, subject to the optimization problems A, B and C are presented. Due to the substantial cost of the objective function, and the requirement to perform many objective evaluations, a parallel decomposition of the population has been developed such that the objective function and constraint evaluations are performed in parallel with one particle assigned to

each core. A master core then performs the optimizer update. The optimizations were ran using 48 particles for a maximum number of 500 iterations.

The final optimized results from each of the four independent optimization runs on each of cases A, B and C are given in tables 2, 3 and 4 respectively, while the convergence histories are given in figure 10. Table 5 gives the mesh converged C_D and eb^2[b] values. These were obtained by coarsening the final mesh that results from the optimization by a factor of two in each dimension and also refining by a factor of two in each dimension. Richardson extrapolation is then performed.

Table 2: Optimization results for case A (C_D in counts)

	C_L	C_D	C_{M_x}	V	s	$S/2$	γ	AoA	$\Delta J(\%)$
Baseline	0.263	43.8	0.116	0.247	3.06	3.02	0.0°	2.99°	-
Run 1	0.263	32.5	0.107	0.247	3.67	3.02	-0.408°	3.80°	**-25.8%**
Run 2	0.263	33.2	0.106	0.247	3.67	3.02	-0.345°	4.34°	**-24.2%**
Run 3	0.263	33.2	0.106	0.247	3.67	3.02	-0.300°	4.18°	**-24.2%**
Run 4	0.263	33.1	0.106	0.247	3.67	3.02	-0.530°	4.34°	**-24.4%**

Table 3: Optimization results for case B (C_D in counts)

	C_L	C_D	C_{M_x}	V	s	$S/2$	γ	AoA	$\Delta J(\%)$
Baseline	0.263	43.8	0.116	0.247	3.06	3.02	0.0°	2.99°	-
Run 1	0.263	31.8	0.105	0.252	3.67	3.02	-0.604°	3.88°	**-27.4%**
Run 2	0.263	32.7	0.102	0.247	3.67	3.02	-0.816°	4.30°	**-25.3%**
Run 3	0.263	31.6	0.106	0.247	3.67	3.02	-0.469°	3.55°	**-27.9%**
Run 4	0.263	31.2	0.105	0.247	3.67	3.02	-0.393°	3.28°	**-28.8%**

Table 4: Optimization results for case C (C_D in counts)

	C_L	C_D	C_{M_x}	V	s	$S/2$	γ	AoA	$\Delta J(\%)$
Baseline	0.263	43.8	0.116	0.247	3.06	3.02	0.0°	2.99°	-
Run 1	0.263	33.4	0.104	0.248	3.53	3.02	-0.697°	4.00°	**-23.7%**
Run 2	0.263	33.2	0.103	0.264	3.64	3.02	-0.427°	3.31°	**-24.2%**
Run 3	0.263	33.5	0.106	0.248	3.67	3.02	-0.511°	3.67°	**-23.5%**
Run 4	0.263	34.8	0.104	0.252	3.67	3.02	-0.632°	4.07°	**-20.5%**

[b]The value of eb^2 is requested in the specification of ADODG case 6[22] to allow a fairer comparison of different results that may occur due to either different meshes or slightly different C_L values.

Table 5: Mesh converged optimization results (C_D in counts)

Case A			Case B			Case C		
Run	C_D	eb^2	Run	C_D	eb^2	Run	C_D	eb^2
Baseline	38.1	34.9	*Baseline*	38.1	34.9	*Baseline*	38.1	34.9
Run 1	26.8	49.4	Run 1	25.5	52.0	Run 1	26.9	49.2
Run 2	26.9	49.2	Run 2	26.2	50.6	Run 2	26.9	49.2
Run 3	27.6	48.0	Run 3	25.1	52.8	Run 3	27.0	49.1
Run 4	26.8	49.4	Run 4	24.7	53.6	Run 4	28.5	46.5
Optimal	24.7	53.6	*Optimal*	24.7	53.6	*Optimal*	24.7	53.6

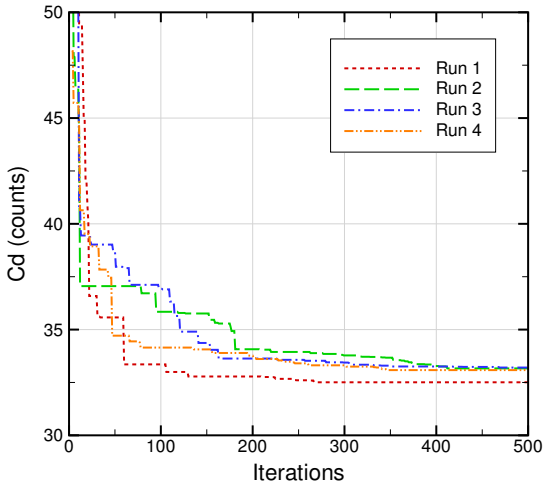

(a) Case A

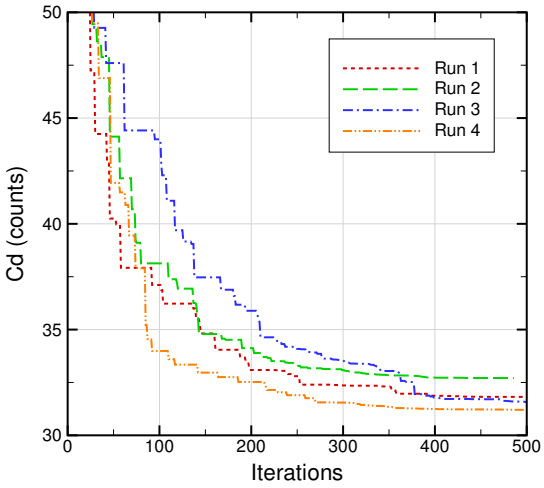

(b) Case B

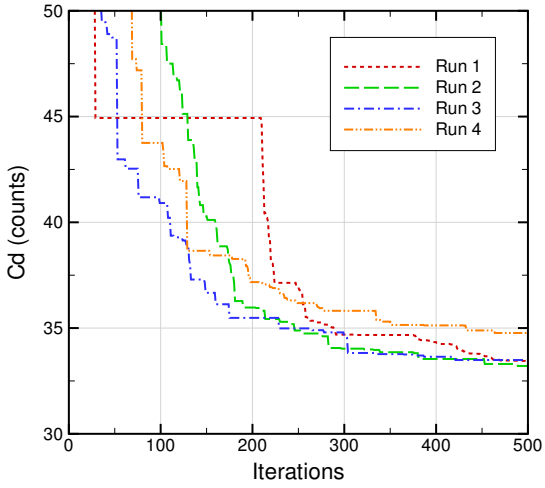

(c) Case C

Figure 10: Convergence histories

It should be noted that the baseline wing is infeasible due to the bending moment constraint being violated, though this appears to not be a problem for the optimizer, which has resulted in final bending

moment values close to active. Of course this is expected since the optimum loading would be elliptical without the bending moment constraint, but the load has to be moved inboard to produce a feasible optimum with an active constraint. Also, as expected, in all cases the lift constraint is active; the wing was not trimmed by the solver through the solution but by the optimizer with an angle of attack variable, so the active constraint is testament to the quality of the optimization framework at finding a minimum. Other, almost universally active constraints are the area, maximum span and volume. An interesting trend is that the twist levels are remarkably low for all of the optimized designs. It appears that the optimizer has used other means (primarily chord) to affect the loading and bring it close to the optimum.

Regarding the objective function and design variable values of the runs, case A clearly demonstrates multimodality when considering the chord variation in isolation. Specifically, the multimodality observed is clearly at least two solutions that are individually identifiable, but have almost exactly the same objective values. Star maps are shown in figures 11 to 13 show the final scaled[c] design variable values for each of the runs. The star map in figure 11 clearly shows that of the four runs, runs 1 and 3 have tended towards one solution (which from figure 15 is a smaller, more uniform chord with a larger 'paddle'-like tip), while runs 2 and 4 have tended towards another solution (which has an increase in chord until about 3/4 span, followed by a sharp reduction in the chord). The loading, shown in figure 14 also demonstrates that although there is chord variation between the two optima, the non-dimensionalised loading is consistent, and very close to the theoretical optimum. It should be noted that the lifting-line theory models the wing as a flat plate whereas the Euler flow models non-linearities around the wing that arise from having a thick body, such as the acceleration around the tip; this produces the oscillations in the loading near the tip that are observed in figure 14.

[c]The scaling converts the design variable into a value between 0 and 1 such that 0 represents that design variable's lower bound and 1 represents the upper bound

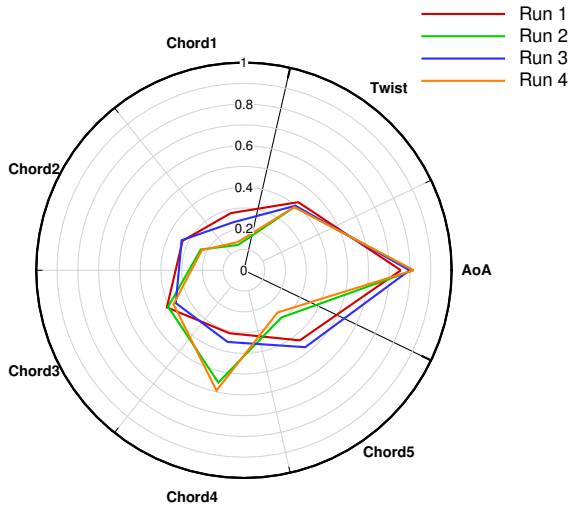

Figure 11: Star map of case A

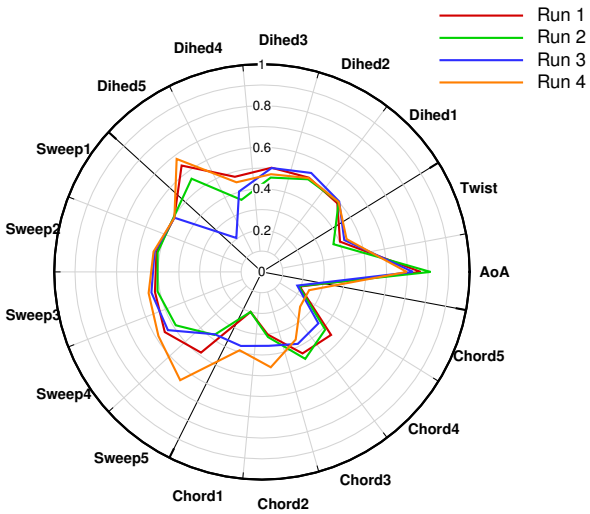

Figure 12: Star map of case B

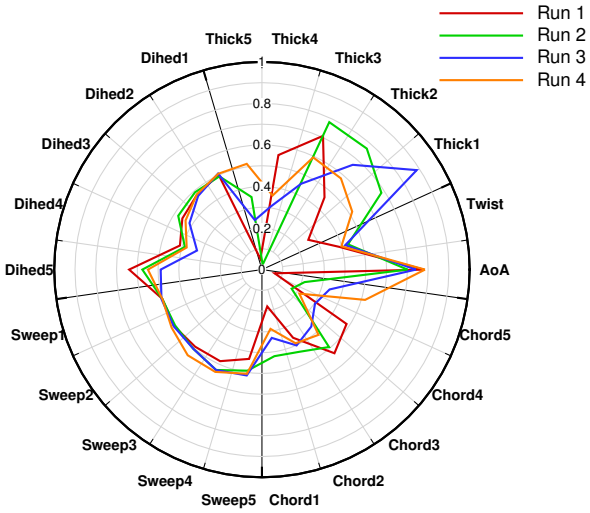

Figure 13: Star map of case C

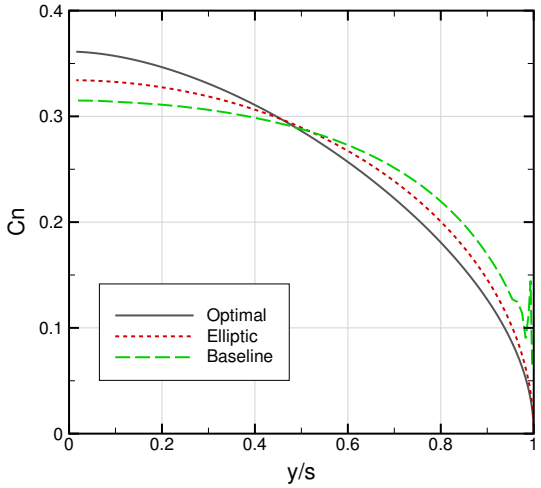

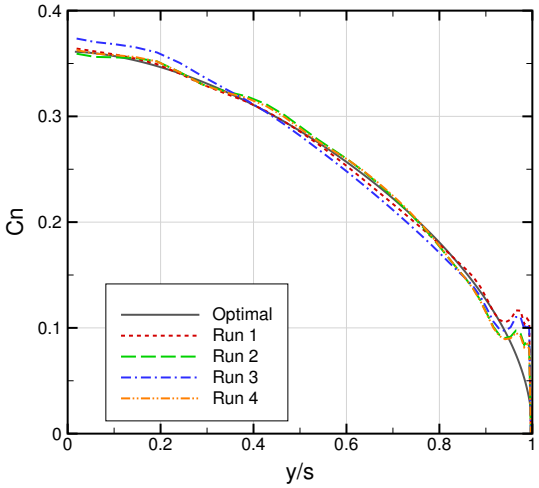

(b) Case A

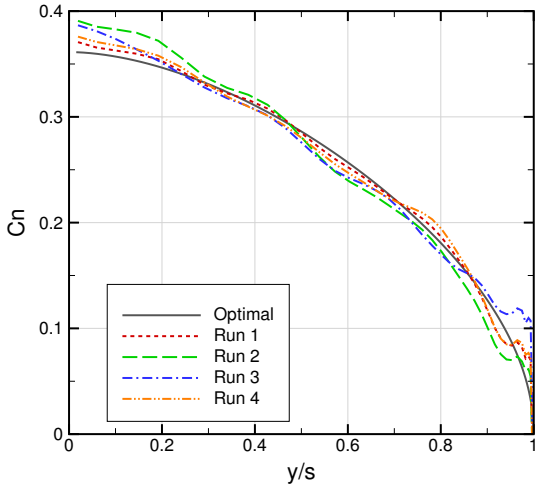

(c) Case B

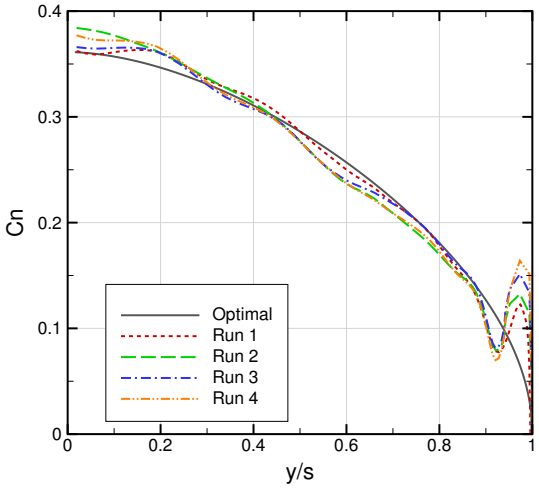

(d) Case C

Figure 14: Span-wise loading

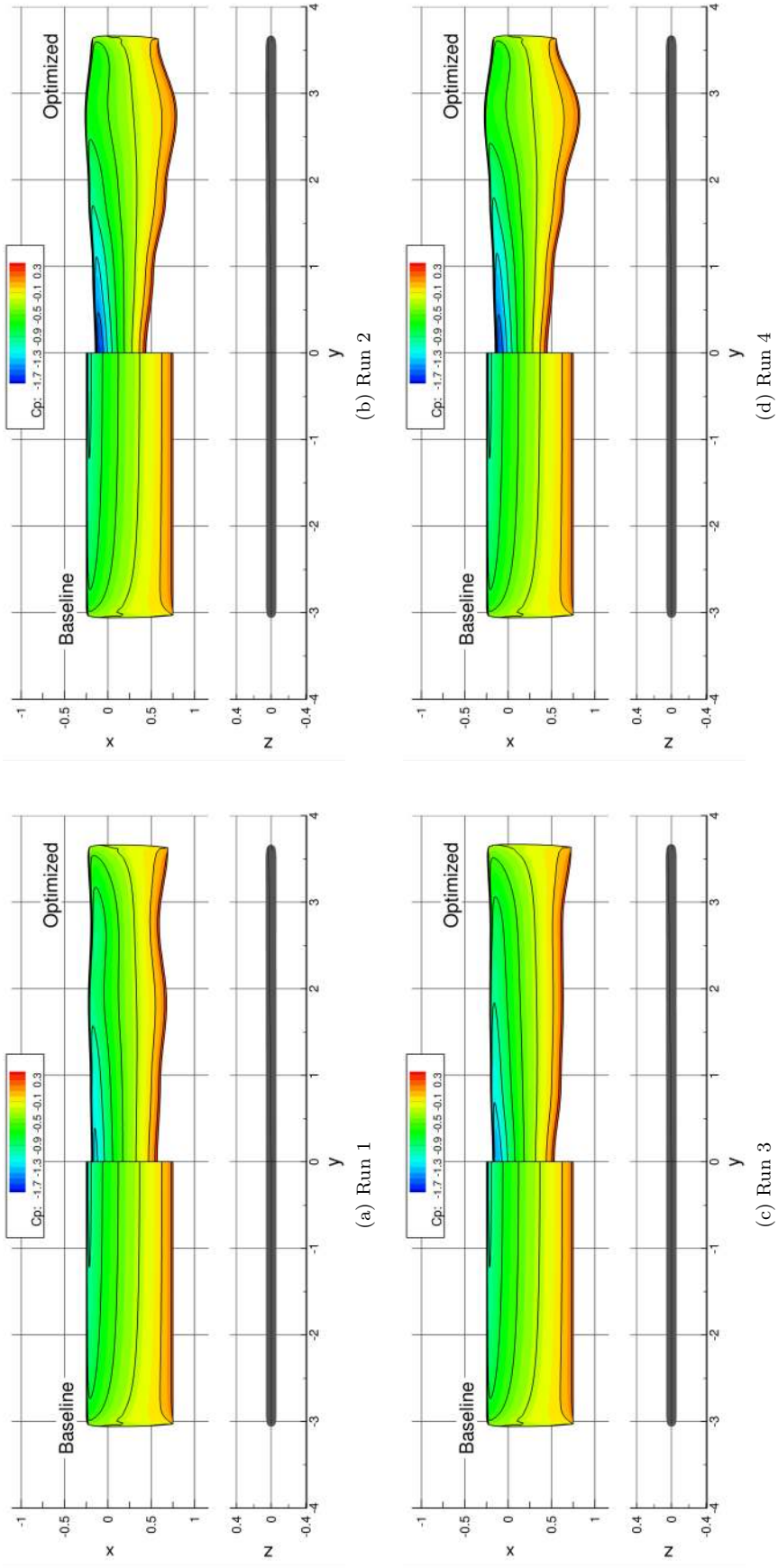

(a) Run 1 (b) Run 2 (c) Run 3 (d) Run 4

Figure 15: Surface shape and upper surface pressure contours for case A

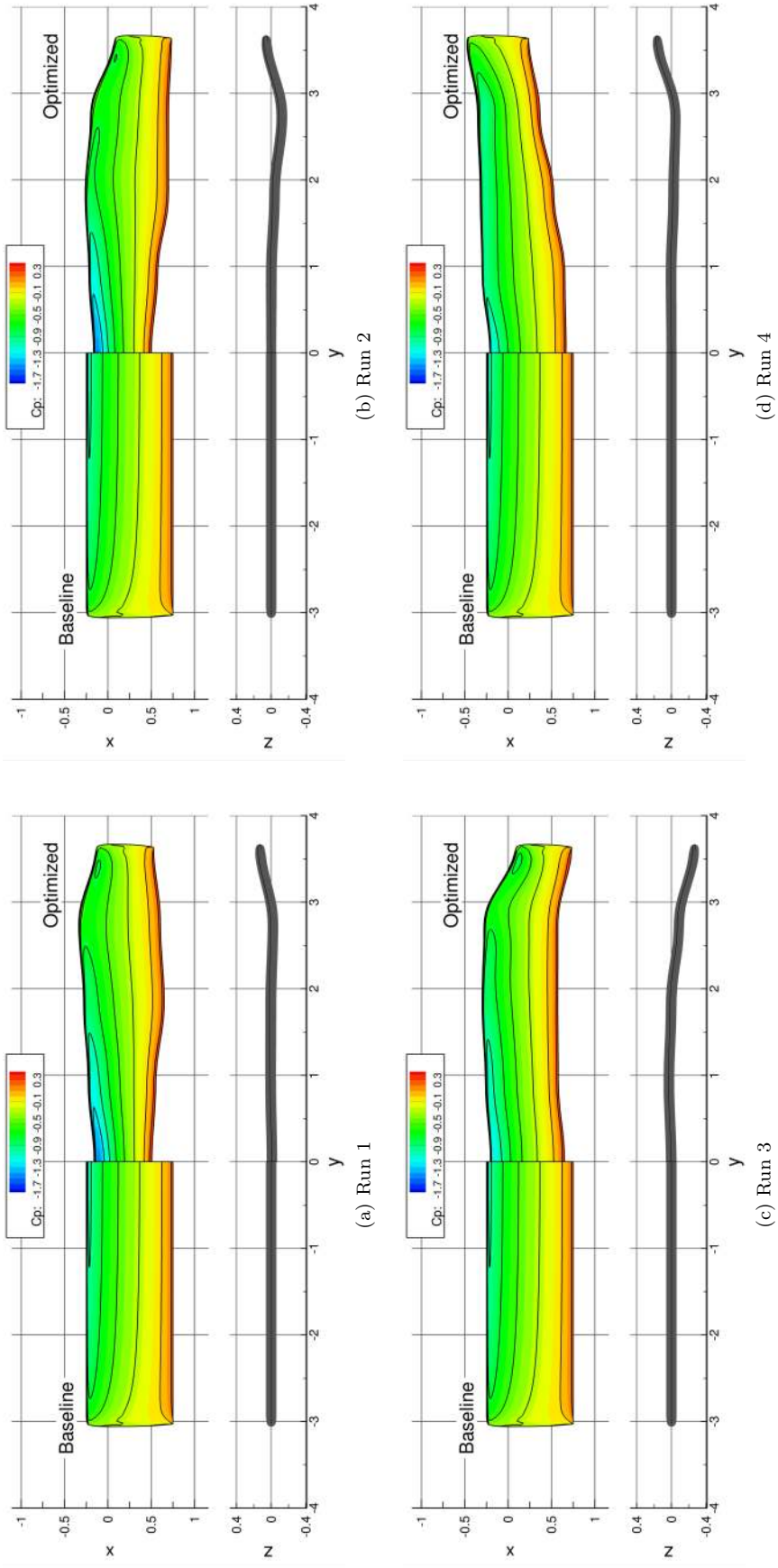

(a) Run 1 (b) Run 2 (c) Run 3 (d) Run 4

Figure 16: Surface shape and upper surface pressure contours for case B

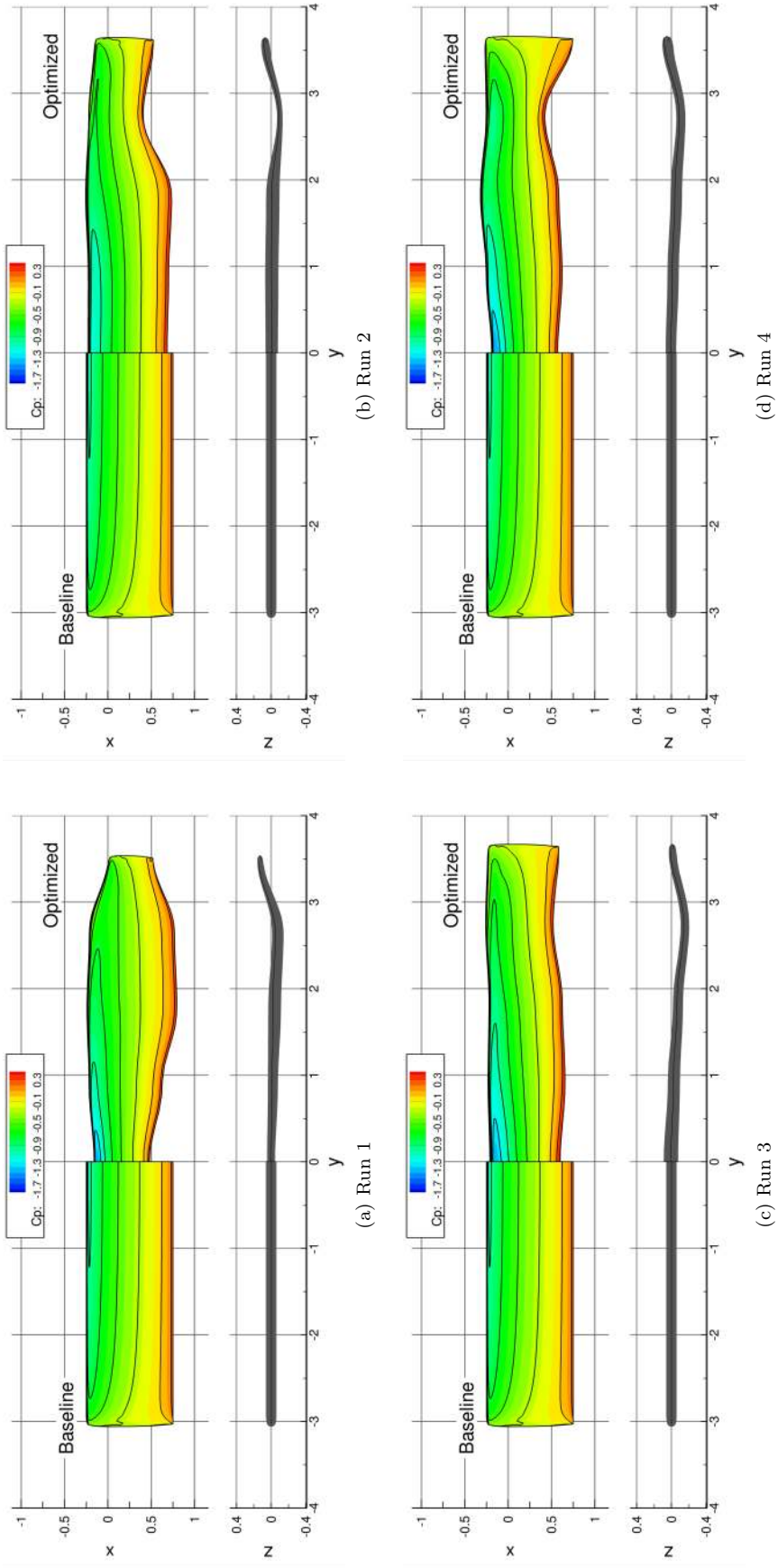

(a) Run 1 (b) Run 2 (c) Run 3 (d) Run 4

Figure 17: Surface shape and upper surface pressure contours for case C

Better optimum drag (and eb^2) values are attainable once horizontal (sweep) and vertical (dihedral) perturbations are introduced. From figure 16, it is clear that when the dihedral design variables are introduced, the wing forms two distinct shapes in the $y-z$ plane. Runs 1, 2 and 4 go towards a shape with little variation in vertical displacement, except close to the tip, where a winglet-like geometry is formed, whilst run 3 goes toward a more parabolic shape with a downward displacement towards the tip. The winglet-like geometry is an expected result since given the span restriction, a reduction in induced drag can be forced. This is in addition to an increase in lift, which leads to a reduction in overall trimmed drag once the wing is then trimmed back to its design condition. The chord variations that were seen in case A are again observed here, with runs 1 and 2 having small root chord and larger mid-span chords, whereas runs 3 and 4 tending toward close to constant chord along the span. There is, though further multimodality introduced in the sweep; runs 1, 2 and 3 have little to no sweep except at the tip, which shows rearward sweep, whereas run 4 is clearly showing forward sweep (and this is demonstrated in the star map of figure 12. The addition of sweep (either forward or backwards) has the effect of increasing the effective chord leading to an increase in lift and again, leading to a decrease in trimmed drag.

The final case (case C) demonstrates the addition of thickness. One obvious trend is that this appears to have the influence of confusing the optimization algorithm, possibly indicating a multimodal design space. The first evidence of this is the final drag results from table 4, which, even though contain the design spaces of runs B and A, are not able to obtain the low drag values of those runs. However, theoretically this could also be due to unconverged optimization runs. Figure 18 gives the convergence of the modulus of the best solution found through the optimization (i.e. $|\mathbf{s}(t)|$), which shows that in the initial iterations, the optimizer performs global search. Towards the end of the optimization runs, little change occurs in the best solution found giving indication that the optimizer has found a minimum that it is happy with. Lack of optimizer convergence does not appear to be the cause of the results of case C having higher drag values than cases B and A, so the conclusion that is drawn is one of a highly multimodal design space.

The multimodality due to the chord variation seen in run A is again, clearly visible in case C, as is that due to sweep. Interestingly, the four runs have all gone towards the winglet-like geometry seen in three of the four runs of case B. This is not to say that the parabolic geometry of run 3 from case B is not a minimum, but that the four runs have resulted in a more consistent geometry. From the star-map of figure 13, it is clear that the differences are coming primarily from the thickness and chord variations. The volume constraint creates a strong coupling between these two variables, so this multimodality is unsurprising.

To further investigate the multimodality, it is useful to consider projected plots of cases A and C in figures 19 and 20. Projected plots show every solution from each of the histories of all of the optimizations (i.e. the objective function of every feasible particle at every iteration) projected in each combination of

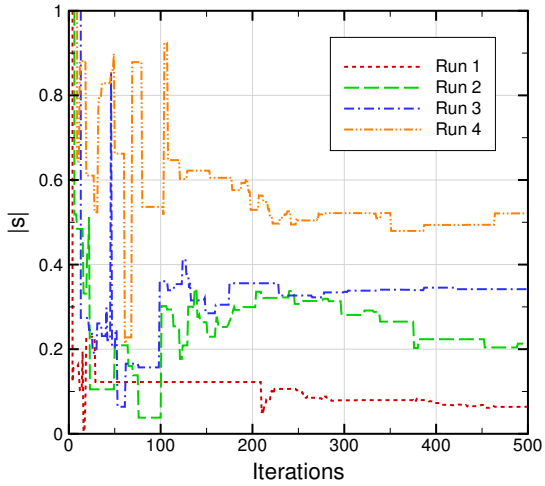

Figure 18: Convergence of $|\mathbf{s}(t)|$ of case C

design variables. This gives a powerful way of visualising any multimodality that may exist. Table 6 gives the definition of each variable symbol in the projected plots.

Table 6: Explanation of variables in projected plots

Variable	Description	y/s location	Lower bound	Upper bound
AoA	Angle of attack	Global	$-3.0°$	$6.0°$
γ	Twist		$-3.12°$	$3.12°$
$t1$	Thickness	0.0	Reduce by 50%	Increase by 50%
$t2$		0.25		
$t3$		0.5		
$t4$		0.75		
$t5$		1.0		
$z1$	Vertical displacement	0.0	Move section down by 0.45	Move section up by 0.45
$z2$		0.25		
$z3$		0.5		
$z4$		0.75		
$z5$		1.0		
$x1$	Horizontal displacement	0.0	Sweep rearwards by 1.0	Sweep forwards by 1.0
$x2$		0.25		
$x3$		0.5		
$x4$		0.75		
$x5$		1.0		
$c1$	Chord	0.0	Decrease by 55%	Increase by 55%
$c2$		0.25		
$c3$		0.5		
$c4$		0.75		
$c5$		1.0		

For case A (shown in figure 19), the twist variation appears to exhibit a single minimum, which is

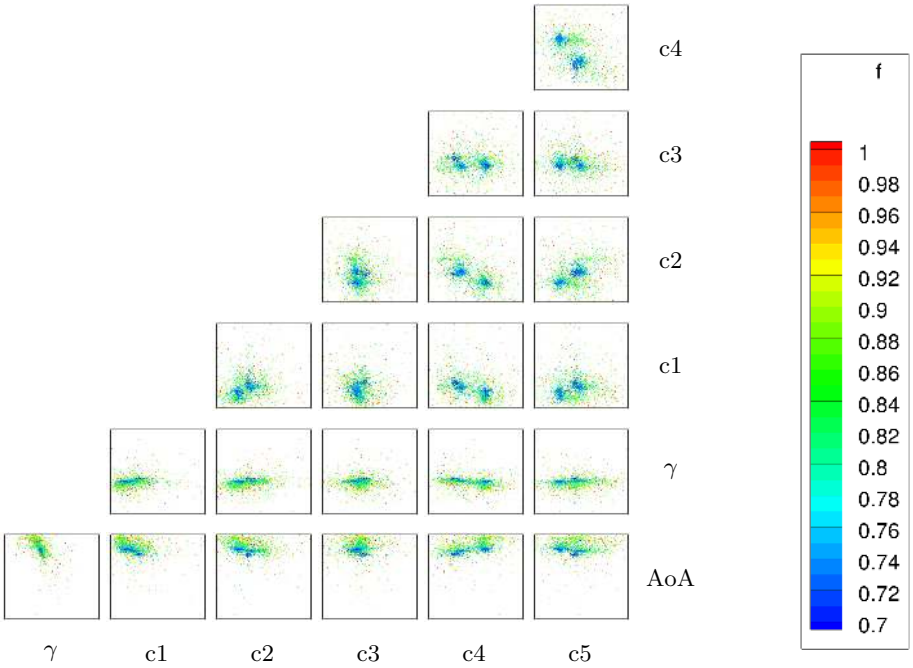

Figure 19: Projected plots of case A (colours represent objective function value)

expected. The first, second and third chord variations all appear to have close to a single minima, which is one where the chord is reduced at the root in an attempt to increase the span as much as possible. On the other hand, when moving towards the tip, the fourth and fifth chord variations are where multimodality is introduced. There are clearly two minima in this space; a reduction in the fourth chord variable with an associated increase in the fifth chord variable, and *vice versa*. The variety in the chord variation closer to the tip is likely down to the need to satisfy the root bending moment constraint. There appears to be no other identifiable feasible minima that have been considered throughout the search history of the other four runs of case A.

For case C (shown in figure 20), the multimodality is striking, and appears in a substantial number of design variable combinations. As already noted, there is very strong coupling between the chord and thickness variations. This is such that the volume constraint is satisfied, but this also leads to variations in the thickness-to-chord ratio which has implications in the spanwise loading. As seen in case A, there is multimodality in the variation of the chord close to the tip. Of course, since the design space of case A is contained within that of case C, this is expected. It is clear that the design space of the full ADODG case 6 (described here by case C) is multimodal, and that this is due to coupling between multiple design variables.

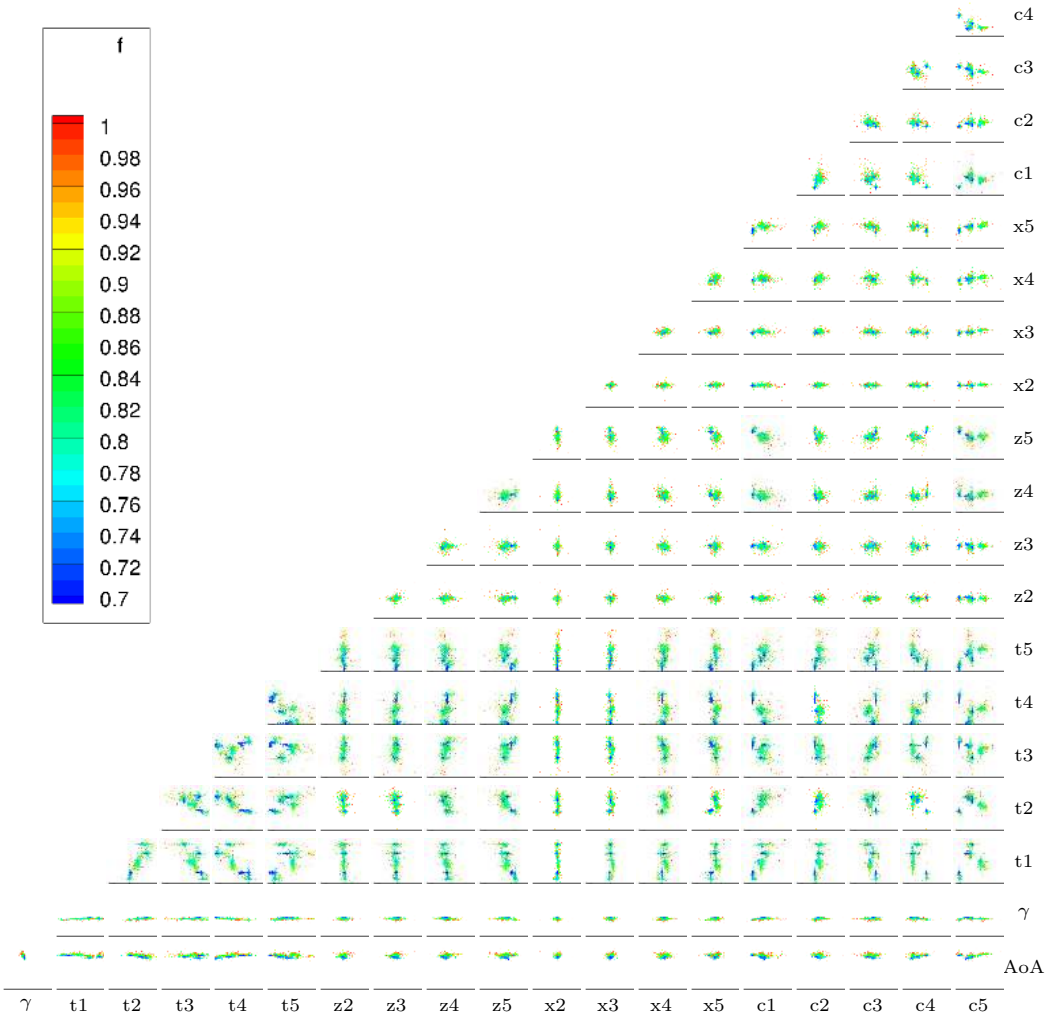

Figure 20: Projected plots of case C (colours represent objective function value)

VI. Conclusions

An investigation of a new ADODG optimization benchmark case has been performed. The problem, which involves drag minimization of a rectangular NACA0012 wing subject to lift and root-bending moment constraints as well as other geometric constraints, such as span and wing area, is believed to exhibit multimodality. In this work, a constrained global optimizer has been used to optimize the wing, with design variables characterised using a hierarchical control point approach to allow an efficient representation of the wing.

The optimizer, which is a global population-based algorithm (a hybrid of particle swarm optimization and gravitational search algorithm) has been run four times, with each run being independent of the others, on three different optimization cases (giving 12 independent optimization runs) representing increasing fidelity of design space: chord and twist; chord, dihedral, sweep and twist; and the full optimization including thickness. The starting location of the particles in each of the runs are distinctive. Furthermore, the global optimizer is stochastic and encourages a balance between design space exploration and optima exploitation.

Elliptical loading of the optimal solution cannot be achieved, and instead a theoretical optimal loading that shifts load inboard to satisfy the root bending moment constraint is optimal, with a corresponding optimum induced drag for the wing at maximum allowable span of 24.7 counts. For all of the optimizations considered, the span goes to the maximum allowable span. When considering chord changes only, two distinct optima are found with very similar drag values (mesh converged values of around 27 counts). When adding dihedral and sweep, further modality is added with the dihedral variation leading to optima with upward and downward winglet-like geometries. Furthermore, both forward and rearward sweep are also observed in the optima of the four runs for this case. This produces optimal geometries close the the theoretical minimum (around 25 counts) Finally, adding thickness has the effect of greatly increasing the modality of the problem probably due to there being a strong coupling between the chord and thickness. Projected plots of the feasible solutions through the optimization process were used to confirm this.

Acknowledgements

The authors kindly acknowledge the support of the EPSRC-supported University of Bristol EPSRC Doctoral Training Grant. This work was carried out using the computational facilities of the Advanced Computing Research Centre, University of Bristol - http://www.bris.ac.uk/acrc/.

References

[1] Poole, D. J., Allen, C. B., and Rendall, T. C. S., "High-fidelity aerodynamic shape optimization using efficient orthogonal modal design variables with a constrained global optimizer," *Computers & Fluids*, Vol. 143, 2017, pp. 1–15.
doi:10.1016/j.compfluid.2016.11.002.

[2] Poole, D. J., Allen, C. B., and Rendall, T. C. S., "Objective Function and Constraints for Robust Transonic Aerofoil Optimization," *58th AIAA/ASCE/AHS/ASC Structures, Structural Dynamics, and Materials Conference*, Dallas, Texas, 2017, AIAA Paper 2017-0360.
doi:10.2514/6.2017-0360.

[3] Hicks, R. M. and Henne, P. A., "Wing Design by Numerical Optimization," *Journal of Aircraft*, Vol. 15, No. 7, 1978, pp. 407–412.
doi:10.2514/6.1977-1247.

[4] Qin, N., Vavalle, A., Le Moigne, A., Laban, M., Hackett, K., and Weinerfelt, P., "Aerodynamic Considerations of Blended Wing Body Aircraft," *Progress in Aerospace Sciences*, Vol. 40, No. 6, 2004, pp. 321–343.
doi:10.1016/j.paerosci.2004.08.001.

[5] Nielsen, E. J., Lee-Rausch, E. M., and Jones, W. T., "Adjoint Based Design of Rotors in a Noninertial Frame," *Journal of Aircraft*, Vol. 47, No. 2, 2010, pp. 638–646.
doi:10.2514/1.46044.

[6] Lyu, Z., Kenway, G. K. W., and Martins, J. R. R. A., "Aerodynamic Shape Optimization Investigations of the Common Research Model Wing Benchmark," *AIAA Journal*, Vol. 53, No. 4, 2015, pp. 968–985.
doi:10.2514/1.J053318.

[7] Choi, S., Lee, K. H., Potsdam, M., and Alonso, J. J., "Helicopter Rotor Design Using a Time-Spectral and Adjoint Based Method," *Journal of Aircraft*, Vol. 51, No. 2, 2014, pp. 412–423.
doi:10.2514/1.C031975.

[8] Morris, A. M., Allen, C. B., and Rendall, T. C. S., "CFD-based Optimization of Aerofoils Using Radial Basis Functions for Domain Element Parameterization and Mesh Deformation," *International Journal for Numerical Methods in Fluids*, Vol. 58, No. 8, 2008, pp. 827–860.
doi:10.1002/fld.1769.

[9] Allen, C. B. and Rendall, T. C. S., "Computational-Fluid-Dynamics-Based Optimisation of Hovering Rotors Using Radial Basis Functions for Shape Parameterisation and Mesh Deformation," *Optimization*

and Engineering, Vol. 14, 2013, pp. 97–118.
doi:10.1007/s11081-011-9179-6.

[10] Masters, D. A., Taylor, N. J., Rendall, T. C. S., Allen, C. B., and Poole, D. J., "Geometric Comparison of Aerofoil Shape Parameterization Methods," *AIAA Journal*, Vol. 55, No. 5, 2017, pp. 1575–1589.
doi:10.2514/1.J054943.

[11] Chernukhin, O. and Zingg, D. W., "Multimodality and Global Optimization in Aerodynamic Design," *AIAA Journal*, Vol. 51, No. 6, 2013, pp. 1342–1354.
doi:10.2514/1.J051835.

[12] Lyu, Z., Xu, Z., and Martins, J. R. R. A., "Benchmarking Optimization Algorithms for Wing Aerodynamic Design Optimization," *Eighth International Conference on Computational Fluid Dynamics (ICCFD8)*, Chegdu, China, 2014, ICCFD8-2014-0203.

[13] Bisson, F. and Nadarajah, S. K., "Adjoint-Based Aerodynamic Optimization of Benchmark Problems," *53rd AIAA Aerospace Sciences Meeting*, Kissimmee, Florida, 2015, AIAA Paper 2015-1948.
doi:10.2514/6.2015-1948.

[14] Poole, D. J., Allen, C. B., and Rendall, T. C. S., "Control Point-Based Aerodynamic Shape Optimization Applied to AIAA ADODG Test Cases," *53rd AIAA Aerospace Sciences Meeting*, Kissimmee, Florida, 2015, AIAA Paper 2015-1947.
doi:10.2514/6.2015-1947.

[15] Meheut, M., Destarac, D., Carrier, G., Anderson, G., Nadarajah, S., Poole, D., Vassberg, J., and Zingg, D., "Gradient-Based Single and Multi-points Aerodynamic Optimizations with the elsA Software," *53rd AIAA Aerospace Sciences Meeting*, Kissimmee, Florida, 2015, AIAA Paper 2015-0263.
doi:10.2514/6.2015-0263.

[16] Lee, C., Koo, D., Telidetzki, K., Buckley, H. P., Gagnon, H., and Zingg, D. W., "Aerodynamic Shape Optimization of Benchmark Problems Using Jetstream," *53rd AIAA Aerospace Sciences Meeting*, Orlando, Florida, 2015, AIAA Paper 2015-0262.
doi:10.2514/6.2015-0262.

[17] LeDoux, S. T., Vassberg, J. C., Young, D. P., Fugal, S., Kamenetskiy, D., Huffman, W. P., Melvin, R. G., and Smith, M. F., "Study Based on the AIAA Aerodynamic Design Optimization Discussion Group Test Cases," *AIAA Journal*, Vol. 53, No. 7, 2015, pp. 1910–1935.
doi:10.2514/1.J053535.

[18] Kenway, G. K. W. and Martins, J. R. R. A., "Multipoint Aerodynamic Shape Optimization Investigations of the Common Research Model Wing," *AIAA Journal*, Vol. 54, No. 1, 2016, pp. 113–128. doi:10.2514/1.J054154.

[19] Ren, J., Thelen, A., Amrit, A., Du, X., Leifsson, L., Tesfahunegn, Y. A., and Koziel, S., "Application of Multifidelity Optimization Techniques to Benchmark Aerodynamic Design Problems," *54th AIAA Aerospace Sciences Meeting*, San Diego, California, 2016, AIAA Paper 2016-1542. doi:10.2514/6.2016-1542.

[20] Masters, D. A., Poole, D. J., Taylor, N. J., Rendall, T. C. S., and Allen, C. B., "Influence of Shape Parameterisation on a Benchmark Aerodynamic Optimisation Problem," *Journal of Aircraft*, Published online. doi:10.2514/1.C034006.

[21] Iuliano, E., "Global optimization of benchmark aerodynamic cases using physics-based surrogate models," *Aerospace Science and Technology*, Vol. 67, 2017, pp. 273–286. doi:10.1016/j.ast.2017.04.013.

[22] Zingg, D. W. and Streuber, G., "Aerodynamic Design Optimization Workshop: Multimodal Subsonic Inviscid Optimization Problem," Tech. rep., AIAA ADODG, 2017, https://info.aiaa.org/tac/ASG/APATC/AeroDesignOpt-DG/Test%20Cases/ADODG%20Case%206%20Multimodal%20Subsonic%20Inviscid%20Optimization.pdf.

[23] Holland, J. H., *Adaptation in Natural and Artificial Systems*, The University of Michigan Press, 1975.

[24] Storn, R. and Price, K., "Differential Evolution - A simple and efficient adaptive scheme for global optimization over continuous spaces," Tech. rep., ICSI, UC Berkeley, 1995, TR-95-012.

[25] Storn, R. and Price, K., "Differential Evolution A Simple and Efficient Heuristic for Global Optimization over Continuous Spaces," *Journal of Global Optimization*, Vol. 11, 1997, pp. 341–359. doi:10.1023/A:1008202821328.

[26] Kennedy, J. and Eberhart, R., "Particle Swarm Optimization," *1995 IEEE International Conference on Neural Networks*, Perth, Australia, 1995. doi:10.1109/ICNN.1995.488968.

[27] Colorni, A., Dorigo, M., and Maniezzo, V., "Distributed Optimization by Ant Colonies," *European Conference on Artificial Life*, Paris, France, 1991.

[28] Rashedi, E., Nezamabadi-pour, H., and Saryazdi, S., "GSA: A Gravitational Search Algorithm," *Information Sciences*, Vol. 179, 2009, pp. 2232–2248.
doi:10.1016/j.ins.2009.03.004.

[29] Zingg, D. W., Nemec, M., and Pulliam, T. H., "A Comparative Evaluation of Genetic and Gradient-based Algorithms Applied to Aerodynamic Optimization," *European Journal of Computational Mechanics*, Vol. 17, 2008, pp. 103–126.
doi:10.3166/remn.17.103-126.

[30] Namgoong, H., Crossley, W., and Lyrintzis, A. S., "Global Optimization Issues for Transonic Airfoil Design," *9th AIAA/ISSMO Symposium on Multidisciplinary Analysis and Optimization*, Atlanta, Georgia, 2002, AIAA Paper 2002-5641.
doi:10.2514/6.2002-5641.

[31] Khurana, M. S., Winarto, H., and Sinha, A. K., "Airfoil Optimisation by Swarm Algorithm with Mutation and Artificial Neural Networks," *47th AIAA Aerospace Sciences Meeting Including the New Horizons Forum and Aerospace Exposition*, Orlando, Florida, 2010, AIAA Paper 2009-1278.
doi:10.2514/6.2009-1278.

[32] Payot, A. D. J., Rendall, T. C. S., and Allen, C. B., "Restricted Snakes: a Flexible Topology Parameterisation Method for Aerodynamic Optimisation," *55th AIAA Aerospace Sciences Meeting*, Dallas, Texas, 2017, AIAA Paper 2017-1410.
doi:10.2514/6.2017-1410.

[33] Du, X., Amrit, A., Thelen, A., Leifsson, L., Zhang, Y., Han, Z.-H., and Koziel, S., "Aerodynamic Design of a Rectangular Wing in Subsonic Inviscid Flow by Surrogate-Based Optimization," *35th AIAA Applied Aerodynamics Conference*, Denver, Colorado, 2017, AIAA Paper 2017-4366.
doi:10.2514/6.2017-4366.

[34] Bons, N. P., He, X., Mader, C. A., and Martins, J. R. R. A., "Multimodality in Aerodynamic Wing Design Optimization," *35th AIAA Applied Aerodynamics Conference*, Denver, Colorado, 2017, AIAA Paper 2017-3753.
doi:10.2514/6.2017-3753.

[35] Poole, D. J., Allen, C. B., and Rendall, T. C. S., "Global Optimization of Multimodal Aerodynamic Optimization Benchmark Case," *35th AIAA Applied Aerodynamics Conference*, Denver, Colorado, 2017, AIAA Paper 2017-4365.
doi:10.2514/6.2017-4365.

[36] Streuber, G. M. and Zingg, D. W., "Investigation of multimodality in aerodynamic shape optimization based on the Reynolds-Averaged Navier-Stokes equations," *35th AIAA Applied Aerodynamics Conference*, Denver, Colorado, 2017, AIAA Paper 2017-3752.
doi:10.2514/6.2017-3752.

[37] Mukesh, R., Pandiyarajan, R., Selvakumar, U., and Lingadurai, K., "Influence of Search Algorithms on Aerodynamic Design Optimisation of Aircraft Wings," *Procedia Engineering*, Vol. 38, 2012, pp. 2155–2163.
doi:10.1016/j.proeng.2012.06.259.

[38] de Falco, I., Della Cioppa, A., Iazzetta, A., and Tarantino, E., "Evolutionary Algorithms for Aerofoil Design," *International Journal of Computational Fluid Dynamics*, Vol. 11, No. 1-2, 1998, pp. 51–77.
doi:10.1080/10618569808940865.

[39] Jahangirian, A. and Shahrokhi, A., "Aerodynamic Shape Optimization Using Efficient Evolutionary Algorithms and Unstructured CFD Solver," *Computers & Fluids*, Vol. 46, 2011, pp. 270–276.
doi:10.1016/j.compfluid.2011.02.010.

[40] Giannakoglou, K. C., "Design of Optimal Aerodynamic Shapes Using Stochastic Optimization Methods and Computational Intelligence," *Progress in Aerospace Sciences*, Vol. 38, 2002, pp. 43–76.
doi:10.1016/S0376-0421(01)00019-7.

[41] Epstein, B. and Peigin, S., "Optimization of 3D Wings Based on Navier-Stokes Solutions and Genetic Algorithms," *International Journal of Computational Fluid Dynamics*, Vol. 20, No. 2, 2006, pp. 75–92.
doi:10.1080/10618560600761601.

[42] Poole, D. J., Allen, C. B., and Rendall, T. C. S., "A Generic Framework for Handling Constraints with Agent-Based Optimization Algorithms and Application to Aerodynamic Design," *Optimization and Engineering*, Published online.
doi:10.1007/s11081-016-9343-0.

[43] Prandtl, L., "Applications of Modern Hydrodynamics to Aeronautics," Tech. rep., NACA, 1923, NACA Report 116.

[44] Jones, R. T., "The Spanwise Distribution of Lift for Minimum Induced Drag of Wings Having a Given Lift and a Given Bending Moment," Tech. rep., NACA, 1950, NACA Report 2249.

[45] Klein, A. and Viswanathan, S. P., "Approximate Solution for Minimum Induced Drag of Wings with Given Structural Weight," *Journal of Aircraft*, Vol. 12, No. 2, 1975, pp. 124–126.
doi:10.2514/3.44425.

[46] Pate, D. J. and German, B. J., "Lift Distributions for Minimum Induced Drag with Generalized Bending Moment Constraints," *Journal of Aircraft*, Vol. 50, No. 3, 2013, pp. 936–946.
doi:10.2514/1.C032074.

[47] Jameson, A., Schmidt, W., and Turkel, E., "Numerical solution of the Euler equations by finite volume methods using Runge Kutta time stepping schemes," *14th Fluid and Plasma Dynamics Conference*, Palo Alto, California, 1981, AIAA Paper 1981-1259.
doi:10.2514/6.1981-1259.

[48] Allen, C. B., "Multigrid Convergence of Inviscid Fixed- and Rotary-Wing Flows," *International Journal for Numerical Methods in Fluids*, Vol. 39, No. 2, 2002, pp. 121–140.
doi:10.1002/fld.282.

[49] Allen, C. B., "Towards Automatic Structured Multiblock Mesh Generation using Improved Transfinite Interpolation," *International Journal for Numerical Methods in Engineering*, Vol. 74, No. 5, 2008, pp. 697–733.
doi:10.1002/nme.2170.

[50] Roy, C. J., "Grid Convergence Error Analysis for Mixed-Order Numerical Schemes," *AIAA Journal*, Vol. 41, No. 4, 2003, pp. 595–604.
doi:10.2514/2.2013.

[51] Morris, A. M., Allen, C. B., and Rendall, T. C. S., "Domain-Element Method for Aerodynamic Shape Optimization Applied to a Modern Transport Wing," *AIAA Journal*, Vol. 47, No. 7, 2009, pp. 1647–1659.
doi:10.2514/1.39382.

[52] Rendall, T. C. S. and Allen, C. B., "Unified Fluid-Structure Interpolation and Mesh Motion Using Radial Basis Functions," *International Journal for Numerical Methods in Engineering*, Vol. 74, No. 10, 2008, pp. 1519–1559.
doi:10.1002/nme.2219.

[53] Rendall, T. C. S. and Allen, C. B., "Efficient Mesh Motion Using Radial Basis Functions with Data Reduction Algorithms," *Journal of Computational Physics*, Vol. 228, No. 17, 2009, pp. 6231–6249.
doi:10.1016/j.jcp.2009.05.013,.

[54] Wendland, H., *Scattered Data Approximation*, Cambridge University Press, 1st ed., 2005.

[55] Allen, C. B., Poole, D. J., and Rendall, T. C. S., "Efficient Modal Design Variables Applied to Aerodynamic Optimization of a Modern Transport Wing," *17th AIAA/ISSMO Multidisciplinary Analysis and*

Optimization Conference, Washington, D.C., 2016, AIAA Paper 2016-3215.
doi:10.2514/6.2016-3215.

[56] Deb, K., "An Efficient Constraint Handling Method for Genetic Algorithms," *Computer Methods in Applied Mechanics and Engineering*, Vol. 186, 2000, pp. 311–338.
doi:10.1016/S0045-7825(99)00389-8.

[57] Deb, K. and Saha, A., "Multimodal Optimization Using a Bi-Objective Evolutionary Algorithm," *Evolutionary Computation*, Vol. 20, No. 1, 2012, pp. 27–62.
doi:10.1162/EVCO_a_00042.